Monthly Notices
of the
ROYAL ASTRONOMICAL SOCIETY

MNRAS **480,** 2743–2756 (2018)
Advance Access publication 2018 July 23

doi:10.1093/mnras/sty1960

A multifrequency radio continuum study of the Magellanic Clouds – I. Overall structure and star formation rates

B.-Q. For,[1,2] L. Staveley-Smith,[1,3] N. Hurley-Walker,[4] T. Franzen,[4] A. D. Kapińska,[1,3,5] M. D. Filipović,[6] J. D. Collier,[6,7,8] C. Wu,[1] K. Grieve,[6] J. R. Callingham,[9] M. E. Bell,[3,10] G. Bernardi,[11] J. D. Bowman,[12] F. Briggs,[13] R. J. Cappallo,[14] A. A. Deshpande,[15] K. S. Dwarakanath,[15] B. M. Gaensler,[3,16,17] L. J. Greenhill,[18] P. Hancock,[3,4] B. J. Hazelton,[19] L. Hindson,[20] M. Johnston-Hollitt,[4,21] D. L. Kaplan,[22] E. Lenc,[3,17] C. J. Lonsdale,[14] B. McKinley,[3,23] S. R. McWhirter,[14] D. A. Mitchell,[3,7] M. F. Morales,[19] E. Morgan,[24] J. Morgan,[4] D. Oberoi,[25] A. Offringa,[7] S. M. Ord,[3,7] T. Prabu,[15] P. Procopio,[23] N. Udaya Shankar,[15] K. S. Srivani,[15] R. Subrahmanyan,[3,15] S. J. Tingay,[3,4] R. B. Wayth,[3,4] R. L. Webster,[3,23] A. Williams,[4] C. L. Williams[24] and Q. Zheng[26]

Affiliations are listed at the end of the paper

Accepted 2018 July 15. Received 2018 June 27; in original form 2018 January 7

ABSTRACT

We present the first low-frequency Murchison Widefield Array (MWA) radio continuum maps of the Magellanic Clouds (MCs), using mosaics from the GaLactic Extragalactic All-Sky MWA (GLEAM) survey. In this paper, we discuss the overall radio continuum morphology between 76 and 227 MHz and compare them with neutral hydrogen maps, 1.4 GHz continuum maps and optical images. Variation of diffuse emission is noticeable across the Large Magellanic Cloud (LMC) but absent across the bar of the Small Magellanic Cloud (SMC). We also measure the integrated flux densities and derive the spectral indices for the MCs. A double power-law model with fixed $\alpha_1 = -0.1$ fit between 19.7 MHz and 8.55 GHz yields $\alpha_0 = -0.66 \pm 0.08$ for the LMC. A power-law model yields $\alpha_{8.55\mathrm{GHz}}^{85.5\mathrm{MHz}} = -0.82 \pm 0.03$ for the SMC. The radio spectral index maps reveal distinctive flat and steep spectral indices for the H II regions and supernova remnants, respectively. We find strong correlation between H II regions and H_α emission. Using a new 150 MHz–H_α relation as a star formation rate indicator, we estimate global star formation rates of 0.068–0.161 $M_\odot$ yr^{-1} and 0.021–0.050 $M_\odot$ yr^{-1} for the LMC and SMC, respectively. Images in 20 frequency bands, and wideband averages are made available via the GLEAM virtual observatory server.

Key words: radiation mechanisms: non-thermal – radiation mechanisms: thermal – Magellanic Clouds – radio continuum: galaxies.

1 INTRODUCTION

The Large and Small Magellanic Clouds (LMC and SMC) lie at a distance of about 50 and 60 kpc (Hilditch, Howarth & Harries 2005; Pietrzyński et al. 2013), respectively, and are among the closest extragalactic neighbours of our Galaxy. The close proximity of the Magellanic Clouds (MCs) provides an ideal laboratory for us to probe different physical mechanisms in great detail. Pioneering studies of the MCs in radio continuum emission date back to the 1950s (see e.g. Mills 1955; Shain 1959). Subsequent studies have been carried out to either focus on individual objects (e.g. supernova 1987A; Zanardo et al. 2010 and references therein) or large-scale radio structure and total radio spectrum of the MCs (Haynes et al. 1991 and references therein; Hughes et al. 2007). Aside from radio continuum studies, there have been many other comprehensive multiwavelength studies to date (see e.g. Jameson et al. 2016). Yet, there is more to learn about these nearby galaxies.

⋆ E-mail: biqing.for@uwa.edu.au

Radio continuum studies probe two main astrophysical properties: non-thermal synchrotron emission that is generated by relativistic charged particles accelerated in magnetic fields; and thermal free–free emission from ionized hydrogen clouds (HII regions; Lisenfeld & Völk 2000). The former partly originates from discrete supernova remnants (SNRs). However, studies have shown that only about 10 per cent of the non-thermal synchrotron emission is originated from SNRs (Lisenfeld & Völk 2000) and about 90 per cent probably due to the propagation of cosmic ray electrons throughout the galaxy disc (Condon 1992) over time-scales of 10 to 100 Myr (Helou & Bicay 1993). The origin of these electrons is unknown, but could mostly still be from SNRs and supernova explosions. Free–free emission originates from the thermal ionized gas in general including the diffuse ionized gas, though it is stronger in HII regions. Since massive stars ($M > 8$ M$_\odot$) have a relatively short lifetime ($<10^8$ yr), this emission therefore traces recent star formation activity.

The intensity of thermal free–free emission is directly proportional to the total number of Lyman continuum photons. In the optically thin regime, the spectrum of a galaxy can generally be described by a power-law function, $S_\nu \propto \nu^\alpha$, where S_ν is the radio flux density at a given frequency, ν, and α is the spectral index (or power-law slope). The spectrum is "flat" when $\alpha \sim -0.1$. Steep spectra with $\alpha \sim -0.8$ are commonly observed in star-forming galaxies (see Marvil, Owen & Eilek 2015 and references therein). Low-frequency turn-over occurs when the optical depth changes from optically thin to optically thick due to absorption process.

With new state-of-the art low-frequency telescopes, such as the Murchison Widefield Array (MWA; Lonsdale et al. 2009; Bowman et al. 2013; Tingay et al. 2013), it is feasible to carry out new continuum surveys with fast survey speeds to probe astrophysical processes at these frequencies. In this paper, we present a multifrequency study of the MCs using data from the GaLactic Extragalactic All-sky MWA (GLEAM) survey (Wayth et al. 2015; Hurley-Walker et al. 2017), the Parkes single-dish radio telescope and radio interferometer data from the Australia Telescope Compact Array (ATCA). In Section 2, we describe the GLEAM observations and data reduction. We show the radio continuum maps of the MCs and discuss their morphology in comparison with the integrated neutral hydrogen (H I) maps and optical images in Section 3. Our analysis and results are presented in Section 4. In Section 5, we derive the global star formation rates. Our investigation of spatial variation of the spectral index among H II regions, a possible turn-over frequency and the production rates of Lyman continuum photons is described in Section 6. Lastly, we present our conclusions and outlook in Section 7.

2 OBSERVATIONS AND DATA REDUCTION

The MWA is a low-frequency radio interferometer operating between 70 and 300 MHz. It was designed to have a wide field of view (15°–50°) and a short-medium baseline distance suitable for detecting the faint redshifted 21-cm spectral line emission from the Epoch of Reionization (EoR), as well as supporting a wide range of other astrophysics applications (Bowman et al. 2013). Phase 1 of MWA consisted of 128 32-dipole antenna tiles that spread across an area of ∼3 km in diameter. We refer the reader to Tingay et al. (2013) for technical details.

The GaLactic Extragalactic All-sky MWA (GLEAM) survey is the main MWA continuum survey that covers the sky south of declination +30° with a frequency range of 72–231 MHz split into five separated sub-bands (Wayth et al. 2015). The data were collected in nightly drift scans, where all frequencies for a single declination strip were observed each night. The data reduction process is described in detailed in Wayth et al. (2015) and Hurley-Walker et al. (2017). To summarize, raw visibility data were processed using COTTER (Offringa et al. 2015), which performs flagging and averaging of the visibility data to a time resolution of 4 s and a frequency resolution of 40 kHz. Subsequent calibration involved the creation of a sky model for each observation, "peeling" to minimize sidelobes from the bright sources, and astrometric correction for ionospheric effects. Lastly, a single mosaic per sub-band is obtained by combining all declination strips from each week of observations. A slight apparent blurring of the point spread function (PSF) is noted due to slightly different ionospheric conditions in the 20–40 observations per pixel. To take this into account, PSF maps are created for each mosaic as a function of position on the sky, with three channels whose pixels represented the major axis, minor axis, and position angle.

We employ the final flux calibrated mosaic imaged with robust weighting of 0 (Briggs 1995) for this study because the theoretical noise is lower than standard GLEAM data reduction, and the brightness sensitivity is higher. Uncertainty in the flux density scale mainly arises from the declination-dependent flux density correction. The systematic uncertainty ($\sigma_{\rm scale}$) is derived as the standard deviation of a Gaussian fit to the residual variation in the ratio of predicted to measured source flux densities. The systematic uncertainties for the studied regions are 8.5 per cent (LMC) and 13 per cent (SMC) (Hurley-Walker et al. 2017).

3 RADIO CONTINUUM MAPS OF THE MAGELLANIC CLOUDS

We present a series of selected GLEAM images of the MCs in Fig. 1. Due to varying PSF across the large area of the MCs images, we derive the synthesized beam sizes by averaging the values of the corresponding PSF map of each band for the analysed area. The typical PSF variation across each field is 15–20 per cent. A summary of the observed central frequency, synthesized beam, pixel area, and average noise level (RMS) for the 20 GLEAM sub-bands images is given in Table 1. We present combined three colour composite images of the LMC and SMC in Fig. 2. Optically thick H II regions appear to be bluer due to their positive steep spectral index ($\alpha \sim 2$; Condon 1992).

The overall radio continuum morphology of the LMC shows a distinct asymmetry, with the eastern side being brighter and compressed. This asymmetry is also visible in the combined single-dish (Parkes) and interferometer (ATCA) H I map (Kim et al. 2003; Staveley-Smith et al. 2003) as shown by the contours in Fig. 3. We note that the compressed side of the LMC is facing the direction of proper motion of the LMC (Kallivayalil et al. 2013; van der Marel & Kallivayalil 2014) and leading the trailing Magellanic Stream. The "arm" structures as seen in the H I map, as well as the 1.4 GHz (Feitzinger et al. 1987) and 4.75 GHz (Haynes et al. 1991) radio continuum maps, are also visible in the MWA images.

The most notable concentration of radio continuum emission is at the largest H II region, 30 Doradus, where the H I column density is high enough to fuel star formation. The lesser explored star-forming complex, N79, in the south-west region of the LMC has recently been reported to possess more than twice the star formation efficiency of 30 Doradus (Ochsendorf et al. 2017). Interestingly, for both N11 and N79 which are among the largest star-forming regions in the LMC, the radio continuum is relatively weak in all GLEAM sub-bands. Other patches of strong emission are also consistent

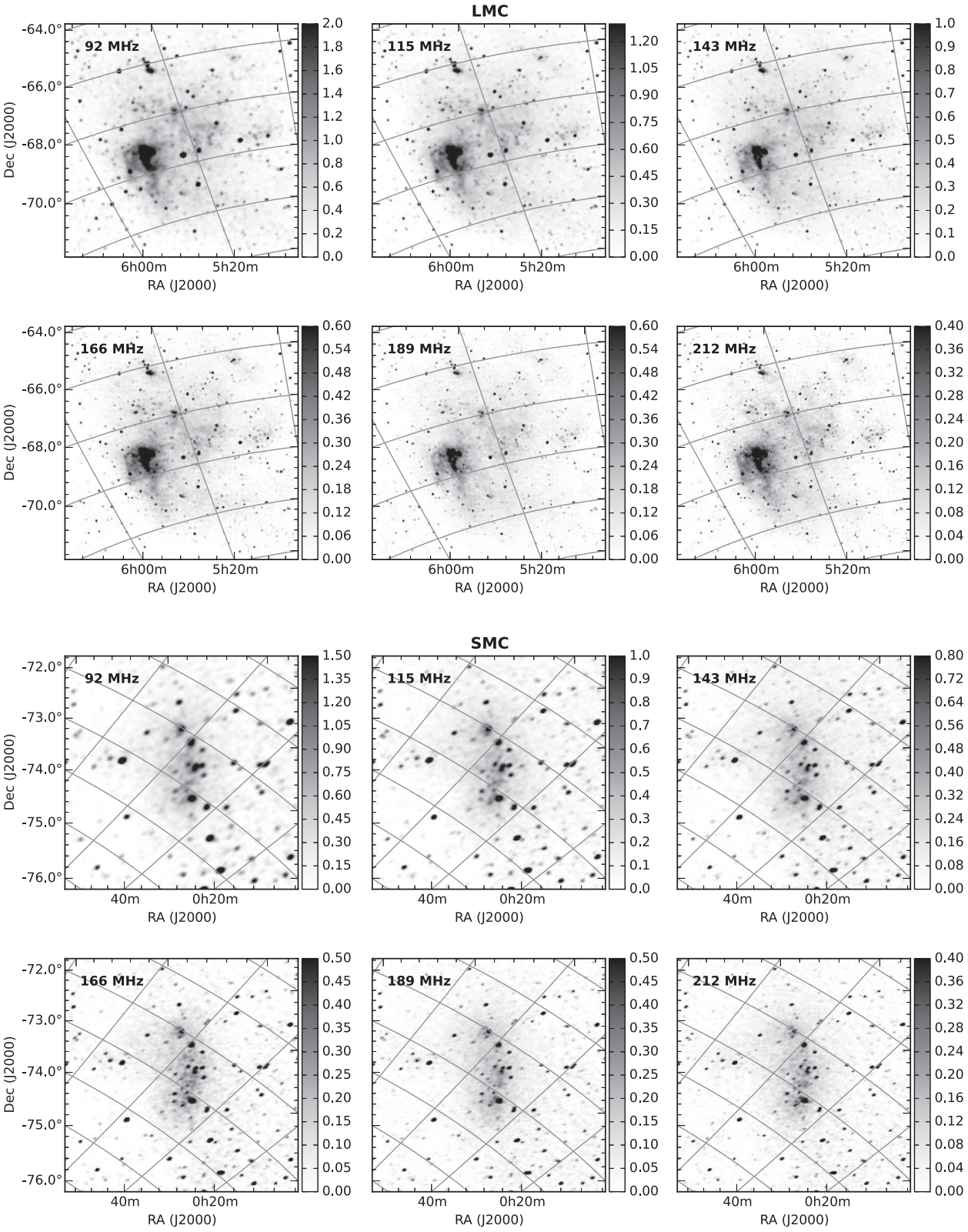

Figure 1. Selected radio images of the LMC and SMC from the GLEAM survey. From top left to bottom right are images centred at 92, 115, 143, 166, 189, and 212 MHz. The grey scale is in units of Jy beam^{-1}.

Table 1. Basic information for the GLEAM images in this study. ν represents the central frequency of the observed sub-band. σ is the average rms of three selected emission free regions. Synthesized beams are derived from the associated PSF map (Section 2).

ν (MHz)	FWHM$_{LMC}$ (arcsec)	FWHM$_{SMC}$ (arcsec)	Pixel Size (arcsec)	σ_{LMC} (Jy beam^{-1})	σ_{SMC} (Jy beam^{-1})
76	471.5 × 411.6	495.4 × 455.6	61.2	0.092	0.079
84	423.5 × 370.5	443.0 × 410.2	61.2	0.056	0.059
92	390.4 × 343.1	407.2 × 378.2	61.2	0.056	0.063
99	367.6 × 319.6	380.4 × 353.9	61.2	0.068	0.055
107	334.5 × 294.5	356.8 × 333.0	45.4	0.041	0.041
115	307.3 × 272.5	328.0 × 306.4	45.4	0.036	0.036
123	289.3 × 256.8	309.8 × 288.2	45.4	0.029	0.032
130	279.6 × 246.6	293.4 × 276.2	45.4	0.030	0.032
143	255.2 × 220.9	271.8 × 255.9	34.9	0.022	0.029
150	240.0 × 208.3	254.4 × 239.5	34.9	0.020	0.025
158	229.3 × 198.8	242.6 × 229.3	34.9	0.019	0.026
166	220.4 × 190.8	234.5 × 222.6	34.9	0.018	0.024
174	212.6 × 184.7	224.5 × 212.6	29.1	0.020	0.025
181	202.4 × 177.2	214.4 × 203.4	29.1	0.018	0.021
189	193.4 × 168.6	208.1 × 196.4	29.1	0.020	0.021
197	188.1 × 163.9	202.1 × 189.4	29.1	0.019	0.020
204	182.0 × 157.9	197.2 × 184.5	25.0	0.018	0.019
212	173.4 × 150.9	189.2 × 176.6	25.0	0.017	0.019
219	169.5 × 147.0	183.4 × 170.4	25.0	0.018	0.019
227	164.8 × 142.9	178.9 × 165.6	25.0	0.017	0.019

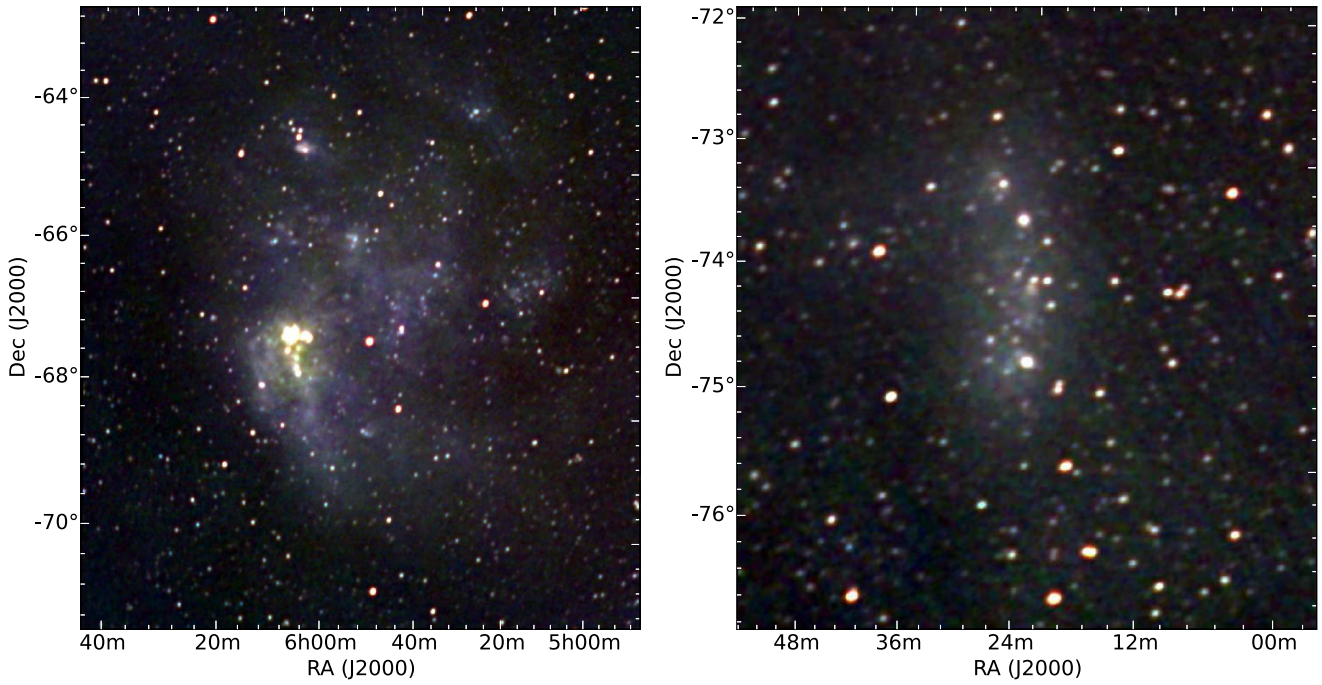

Figure 2. Three colour RGB composite images of the Magellanic Clouds using the combination of 123, 181, and 227 MHz images, respectively. Images are reprojected and regridded to a common projection and angular resolution of 123 MHz images prior to combination. *Left:* Large Magellanic Cloud in a 10° × 10° image, *Right:* Small Magellanic Cloud in a 6° × 6° image.

with supershell locations, where the shell interaction and expansion could also be triggering star formation.

An asymmetry is also seen in deep optical images of the LMC (Besla et al. 2016), except that the overdensity of the stellar component is located at the opposite side (west) of the radio continuum emission. Since the old stellar population results in this overdensity on the western side of the LMC, detection of radio continuum emission is not expected. The asymmetric feature as shown in both radio and optical has been studied in simulations and concluded to be evidence of tidal interaction between our Milky Way and the MCs and a result of ram-pressure (see Diaz & Bekki 2011; Besla et al. 2016; Mackey et al. 2016).

Fig. 3 (bottom panel) shows the 227 MHz radio continuum image of the SMC overlaid with HI contours (Stanimirovic et al. 1999). The overall morphology of the SMC's radio continuum emission is similar to H I, its stellar distribution, and with the dominant of

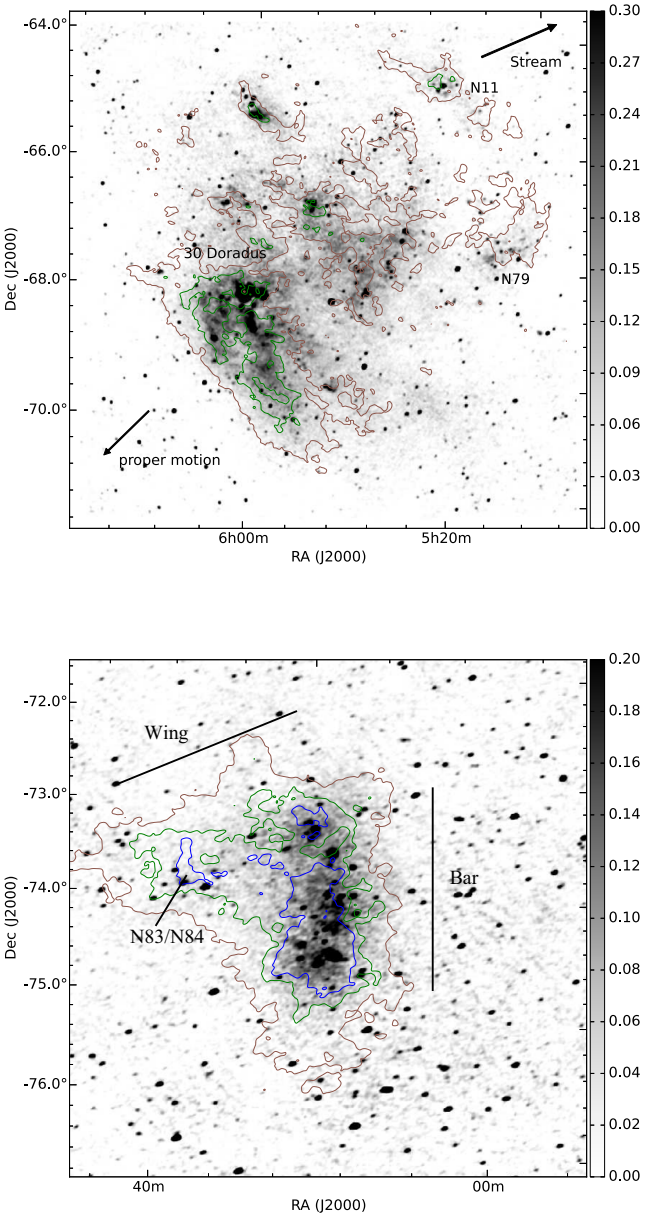

Figure 3. *Top:* H I column density contours (Kim et al. 2003; Staveley-Smith et al. 2003) at 2×10^{21} cm^{-2} (brown) and 4×10^{21} cm^{-2} (green) are overlaid on to the 227 MHz GLEAM radio continuum map of the LMC. The HI map is convolved and regridded to match the resolution and pixel scale of the 227 MHz GLEAM image. The grey scale is in units of Jy beam^{-1}. The directions of proper motion and the Magellanic Stream are indicated by arrows. Extended H I and radio continuum emission south of 30 Doradus point toward the Magellanic bridge and the SMC. *Bottom:* As top, with the addition H I column density contour level at 6×10^{21} cm^{-2} for the SMC (Stanimirovic et al. 1999). The bar and wing are labelled.

bright H II complexes across the bar. There is visible diffuse emission extending out from the bar region toward the south-east side (SMC wing) and the H II complexes (N83/84; Bolatto et al. 2003). The further extensions known as the SMC "tail" (Stanimirovic et al. 1999) and Magellanic bridge (Brüns et al. 2005) are quite distinct in H I. A stellar component has been found in the bridge suggesting stripped material due to tidal interaction (Harris 2007) but the young stellar component also suggests ongoing star formation (Chen et al. 2014).

4 ANALYSIS AND RESULTS

4.1 Integrated flux densities

To obtain the spatially integrated flux densities (S_ν), we extract 8° × 8° and 6° × 6° images centred on the LMC and SMC, respectively, from the mosaic in each band. Subsequently, we mask out pixels below 3σ background noise level of the extracted GLEAM images. The background noise level ($\sigma_{\rm RMS}$) is the average of measured values of three selected emission-free regions around the MCs. The same regions are used for all bands. The S_ν is then calculated using

$$S_\nu = \frac{S_{\nu_{\rm total}} \times p^2}{1.133\ \theta_a\ \theta_b}, \quad (1)$$

where $S_{\nu_{\rm total}}$ is the total flux density (Jy) of the 8° × 8° (LMC) or 6° × 6° (SMC) image, p is the pixel size, θ_a and θ_b are the full-width-half-maximum (FWHM) of the telescope beam's major and minor axis (refer Table 1). We also measure S_ν from archival 1.4 GHz (Hughes et al. 2007) and 4.8 GHz (Haynes et al. 1991) images of the LMC. As for the SMC, archival 1.4 GHz (Staveley-Smith et al. 1997) and 2.37 GHz (Filipović et al. 2002) images are also used for determining S_ν. The same integration areas as those applied to the GLEAM images are used to determine S_ν for the archival data. The 4.8 GHz LMC image and 2.37 GHz SMC image were observed by the single-dish Parkes 64-m telescope. Both 1.4 GHz images of the LMC and SMC are combined single-dish and interferometer data. All measurements are brought to the same absolute flux density scale of Baars et al. (1977).

The errors for the measured integrated flux density are determined using

$$\sigma_{\rm total} = \sqrt{(\sigma_{\rm image})^2 + (\sigma_{\rm scale})^2}, \quad (2)$$

where $\sigma_{\rm image}$ is equal to $\sigma_{\rm RMS} \times \sqrt{N}$, N is the integrated area in units of the synthesized beam area, and $\sigma_{\rm scale}$ is the systematic uncertainty in the flux scale (see Section 2).

Tables 2–3 summarize our measurements and values obtained from the literature at other frequencies. We note that flux densities at 85.5 and 96.8 MHz in Mills (1959) revised by Klein et al. (1989) are significantly higher than our measurements despite these values have been scaled to match the flux density scale of Baars et al. (1977) and corrected for unrelated foreground and background sources. Despite this discrepancy, we still include 85.5 and 96.8 MHz values in our spectral fitting.

The LMC is located in a region of sky in which the Galactic foreground emission is negligible at MHz and GHz frequencies. However, extended Galactic foreground emission is known to be present at the location of the SMC (see discussion in Haynes et al. 1991 and references therein). Examining the SMC region in the 408 MHz all-sky survey of (Haslam et al. 1981), we find that the strongest Galactic foreground emission is located beyond the 6° × 6° region that we use in this study. Measurements of Haynes et al. (1991) have taken into account for the extended Galactic foreground emission because of the larger imaging area than ours. Their studies were conducted using a single-dish telescope. With the use of interferometer data from the MWA, it is possible to resolve out flux from large-scale structure. Based on the shortest baseline of phase I MWA (7.7 m), the largest angular scales for 76 MHz and 227 MHz are 29° and 10°, respectively. Since these angular scales are larger than our studied regions, we do not expect our measurements to be affected by missing flux in the GLEAM images.

Table 2. Integrated flux densities (S_ν) of the Large Magellanic Cloud.

ν (MHz)	S_ν (Jy)	σ (Jy)	Reference
19.7	5270	1054	Shain (1959)[a]
45	2997	450	Alvarez, Aparici & May (1987)
85.5	3689	400	Mills (1959)[a]
96.8	2839	600	Mills (1959)[a]
158	1736	490	Mills (1959)[a]
76	1855.3	315.6	This study
84	1775.7	302.0	This study
92	1574.9	267.9	This study
99	1451.6	247.0	This study
107	1827.6	310.8	This study
115	1627.5	276.8	This study
123	1643.3	279.4	This study
130	1571.8	267.3	This study
143	1663.7	282.9	This study
150	1450.1	246.6	This study
158	1350.4	229.6	This study
166	1204.3	204.8	This study
174	1341.4	228.1	This study
181	1247.1	212.1	This study
189	1223.9	208.1	This study
197	1109.8	188.8	This study
204	1235.3	210.1	This study
212	1121.6	190.8	This study
219	1032.4	175.6	This study
227	1019.7	173.4	This study
408	925	30	Klein et al. (1989)
1400	384	30	This study[b]
1400	529	30	Klein et al. (1989)
2300	412	50	Mountfort et al. (1987)
2450	390	20	Haynes et al. (1991)
4750	363	30	Haynes et al. (1991)
4750	300	40	This study[c]
8550	270	35	Haynes et al. (1991)

Notes. [a]Values revised by Klein et al. (1989).
[b]Using image from Hughes et al. (2007).
[c]Using image from Haynes et al. (1991).

Table 3. Integrated flux densities (S_ν) of the Small Magellanic Cloud.

ν (MHz)	S_ν (Jy)	σ (Jy)	Reference
85.5	460	200	Mills (1955, 1959)[a]
76	403.9	105.2	This study
84	291.4	76.0	This study
92	249.8	65.3	This study
99	262.2	68.5	This study
107	354.4	92.3	This study
115	270.5	70.5	This study
123	257.3	67.0	This study
130	244.1	63.6	This study
143	324.6	84.5	This study
150	258.3	67.3	This study
158	264.1	68.8	This study
166	217.1	56.6	This study
174	356.6	92.8	This study
181	282.8	73.6	This study
189	250.4	65.2	This study
197	246.8	64.3	This study
204	291.4	75.9	This study
212	230.7	60.1	This study
219	219.5	57.2	This study
227	215.2	56.1	This study
408	133	10	Loiseau et al. (1987)
1400	42	6	Loiseau et al. (1987)[b]
1400	34.7	2.0	This study[c]
2300	31	6	Mountfort et al. (1987)
2300	27.1	7.0	This study[d]
2450	26	3	Haynes et al. (1991)
4750	19	4	Haynes et al. (1991)
8550	15	4	Haynes et al. (1991)

Notes. [a]Values revised by Loiseau et al. (1987).
[b]Values revised by Haynes et al. (1991).
[c]Using image from Staveley-Smith et al. (1997).
[d]Using image from Filipović et al. (2002).

4.2 SED modelling

The radio spectrum of a galaxy can normally be approximated by a power-law function, whose slope depends on the thermal and non-thermal nature of the emission. At low-radio frequencies, the spectrum can turn over due to several absorption mechanisms. In the case of the MCs, where there is no evidence of a turn-over, modelling of spectral energy distribution (SED) can take the general forms as described below. We fit the SEDs of the MCs with (a) a power law or (b) a curved power law, or (c) a double power law. A power law is defined as

$$S_\nu = S_0 \left(\frac{\nu}{\nu_0}\right)^\alpha, \tag{3}$$

or in logarithmic form as

$$\log_{10}(S_\nu) = \log_{10}(S_0) + \alpha \log_{10}\left(\frac{\nu}{\nu_0}\right), \tag{4}$$

where ν_0 is the reference frequency, S_0 is the flux density at the reference frequency, and α is the spectral index. A curved power law extends the power law to a quadratic function in logarithmic form that allows for a curvature parameter, c,

$$\log_{10}(S_\nu) = \log_{10}(S_0) + \alpha \log_{10}\left(\frac{\nu}{\nu_0}\right) + c \log_{10}\left(\frac{\nu}{\nu_0}\right)^2. \tag{5}$$

To take into account any "flattening" of the spectrum, we can fit the spectrum with a double power-law model, with the first and second component identified by subscripts 0 and 1. These two components generally represent the synchroton (non-thermal) and free–free (thermal) spectral indices. The model is defined as

$$S_{\rm tot} = S_0 \left(\frac{\nu}{\nu_0}\right)^{\alpha_0} + S_1 \left(\frac{\nu}{\nu_0}\right)^{\alpha_1}. \tag{6}$$

In the optically thin regime, thermal free–free emission from thermal electrons is often characterized by $\alpha = -0.1$ (Klein et al. 1989). We fit the spectra by allowing α_0 and α_1 as free parameters and also by setting a fixed $\alpha_1 = -0.1$ (thermal). A reference frequency of 200 MHz is used throughout the modelling. We also adopt non-linear least squares Lavenberg–Marquardt algorithm for the fitting. We found it necessary to scale the MWA errors by a factor of two to prevent the MWA data points from dominating the overall fit. We refer readers to Harvey et al. (2018) for a detailed description and caveats on SED modelling.

4.2.1 *Model selection*

To select the best model, we first calculate the $\chi^2_{\rm red}$, given by

$$\chi^2_{\rm red} = \frac{\chi^2}{\rm dof} = \frac{\chi^2}{N-k}, \tag{7}$$

where dof is the degree of freedom, N is the number of data points, and k is the number of fitted parameters. We also calculate the Bayesian Information Criterion (BIC; Schwarz 1978), which is defined as

$$BIC = k\ln(N) - 2\ln\hat{L}, \tag{8}$$

$$\hat{L} = \prod_{i=1}^{N} \frac{1}{\sigma_i\sqrt{2\pi}} \exp\left(-\frac{1}{2\sigma_i^2}(S_{\nu_i} - f(\nu_i))^2\right), \tag{9}$$

where $\hat{L}$ is the likelihood function, k and N are the same parameters as in equation (7), S_{ν_i} and σ_i are flux density and uncertainty at frequency ν, respectively. For comparing the two models, a ΔBIC $=$ BIC$_{\rm m1}$ $-$BIC$_{\rm m2}$ is calculated. If ΔBIC is positive, it is in favour of model 2. The model with the lowest BIC is preferred and ΔBIC needs to be > 2 to be statistical significant (Kass & Raftery 1995). Our sequence of comparison starts from the first model and iteratively moves to the next model.

Based on the ΔBIC values, we find the preferred model to be the double power law with fixed $\alpha_1 = -0.1$ (model 3) for the LMC. This model yields $\alpha_0 = -0.66 \pm 0.08$ (non-thermal). This suggests that synchrotron radiation dominates at lower frequencies and thermal free–free emission takes over at higher frequencies. For the SMC, ΔBIC values of model 2–4 are negative which implies the power law (model 1) is the preferred model. A summary of the SED fitting results and associated statistical values is given in Table 4. Fig. 4 shows the best fitting models for the LMC and SMC, respectively.

4.2.2 *Comparison with previous studies*

The derived non-thermal spectral index ($\alpha_0 = -0.66 \pm 0.08$) between 19.7 MHz and 408 MHz, for the LMC is consistent with Klein et al. (1989), $\alpha_{2.3\ \rm GHz}^{19.7\ \rm MHz} = -0.70 \pm 0.06$. For the SMC, we derive $\alpha_{8.55\ \rm GHz}^{85.5\ \rm MHz} = -0.82 \pm 0.03$, which is also consistent with the literature value of $\alpha_{8.55\ \rm GHz}^{85.5\ \rm MHz} = -0.85 \pm 0.05$ (Haynes et al. 1991). Comparing our derived spectral index of the SMC to the mean spectral index derived from all sources in the SMC ($\alpha_{\rm SMC} = -0.73 \pm 0.05$; Filipovic et al. 1998), we do not find significant differences.

4.3 Intensity variation across the MCs

In Section 3, we show that the LMC exhibits an asymmetric morphology in the radio continuum map. We examine the intensity variation across the LMC in 10 MWA frequency bands (see Fig. 5). By dissecting the disc of the LMC through the 30 Doradus region, we find that there are a few peaks associated with the H II regions and supernova remnants. The diffuse emission exhibits constant intensity on the eastern side. A gradual decline in intensity from right ascension $\sim 5^h16^m48^s$ onward to the western end is noticeable. In the north–south direction, the intensity of diffuse emission declines when moving away from the 30 Doradus region. A steeper decline of intensity south of 30 Doradus is seen as compared to the northern part. Compared with the 1.4 GHz radio continuum intensity profiles as shown in fig. 7 of Hughes et al. (2007), the north–south intensity profile is quite similar. We examined the intensity profiles across the bar and north–south direction of the SMC (not shown here), which show that there is no variation apart from a few intensity peaks contributed by the H II regions.

4.4 Contribution from background radio sources

The areas we use for measuring the total flux densities of the MCs include background radio sources. The contribution from the background radio sources can be estimated using a median filtering method. This method has been shown to be successful in eliminating most of the background point sources in the 1.4 GHz radio continuum image (Hughes et al. 2007). Sources intrinsic to the MCs, such as the H II regions, are more compact and not point like. Thus, median filtering will not eliminate them. We perform the median filtering of GLEAM images using the FMEDIAN task in the FTOOLS package[1] (Blackburn 1995). The task convolves an image with a median value within a defined box. Various smoothing window parameters have been tested and we find that the optimal smoothing window for median filtering most of the background sources is 17 × 17 pixels in size. Subsequently, the median-filtered maps are compared to their corresponding non-filtered maps. The results suggested a ∼10 per cent of flux contribution from background sources at the lowest frequency band of GLEAM and ∼20 per cent

Table 4. A summary of the fits to the SED of the MCs using four different models discussed in the text. The reference frequency is 0.2 GHz.

	LMC	SMC
	Power law Model 1	
χ^2	61.5	32.3
$\chi^2_{\rm red}$	2.0	1.2
BIC	466.6	297.9
dof	31	27
S_0	1258.2 ± 43.0 Jy	192.2 ± 9.6 Jy
α	-0.47 ± 0.02	-0.82 ± 0.03
	Curved power law Model 2	
χ^2	55.3	29.3
$\chi^2_{\rm red}$	1.8	1.1
BIC	464.0	298.3
ΔBIC	2.6	−0.4
dof	30	26
S_0	1265.5 ± 41.6 Jy	191.3 ± 9.2 Jy
α	-0.49 ± 0.02	-0.85 ± 0.03
c	0.73 ± 0.10	0.33 ± 0.09
	Double power law, fixed $\alpha_1 = -0.1$ Model 3	
χ^2	52.1	31.8
$\chi^2_{\rm red}$	1.7	1.2
BIC	460.8	300.8
ΔBIC	5.8	−2.9
dof	30	26
S_0	982.6 ± 97.5 Jy	186.4 ± 13.7 Jy
α_0	-0.66 ± 0.08	-0.86 ± 0.08
S_1	265.8 ± 77.5	4.6 ± 7.8
	Double power law Model 4	
χ^2	51.2	28.8
$\chi^2_{\rm red}$	1.8	1.2
BIC	463.3	301.2
ΔBIC	3.3	−3.3
dof	29	25
S_0	1234.0 ± 114.4 Jy	193.0 ± 9.4 Jy
α_0	-0.55 ± 0.09	-0.83 ± 0.05
S_1	28.6 ± 91.9 Jy	0.02 ± 0.20 Jy
α_1	0.41 ± 0.78	1.56 ± 2.65

[1] http://heasarc.gsfc.nasa.gov/ftools/

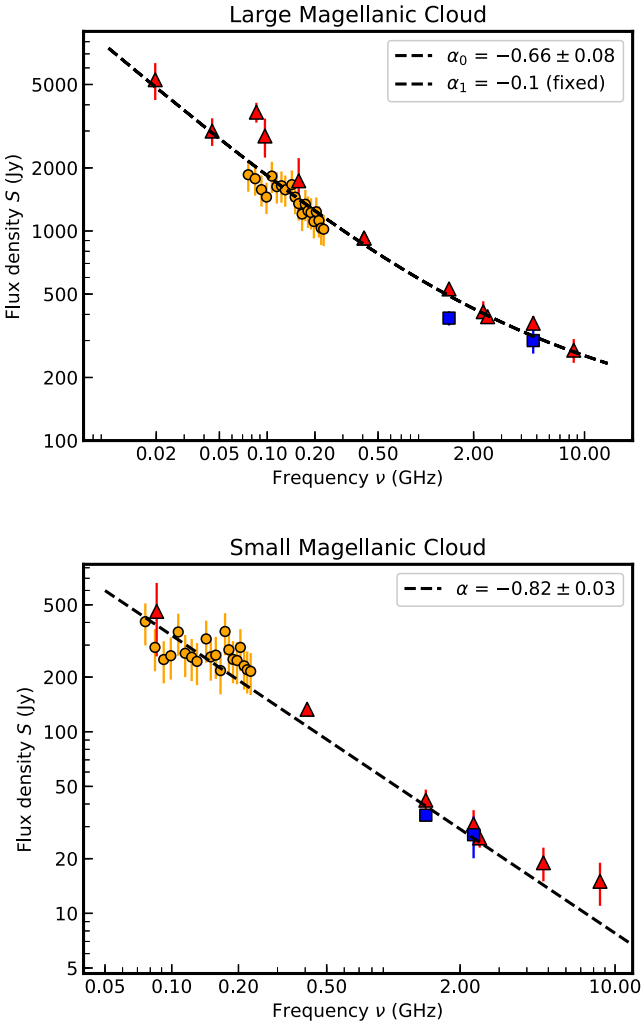

Figure 4. Spectral energy distribution of the Large (top) and Small (bottom) Magellanic Cloud. Orange circles, red triangles, and blue squares represent MWA, values from the literature and re-derived measurements in this study, respectively (refer to Tables 2–3). *Top*: A double power-law model, with $\alpha_0 = -0.66 \pm 0.08$ and $\alpha_1 = -0.1$, is fitted to the LMC spectrum as shown by black dashed line. *Bottom*: A power law with $\alpha = -0.82 \pm 0.03$ is fitted to the SMC spectrum.

at the highest frequency band. We note that the difference in background sources contribution between lowest and highest GLEAM frequency band is probably due to resolution effect given that the spectral index of background sources is independent of frequency. Since this filtering method does not distinguish background point sources and point sources intrinsic to the MCs (Hughes et al. 2007), we do not subtract the contribution when measuring the total integrated flux densities.

4.5 Radio spectral index maps

The spectral index maps allow us to separate the thermal and non-thermal emission of the MCs. We use all GLEAM images but only present the spectral index maps from the GLEAM 166 MHz and the 1.4 GHz images. The GLEAM 166 MHz image is chosen because of its intermediate sensitivity and resolution that emphasizes both diffuse emission and discrete sources.

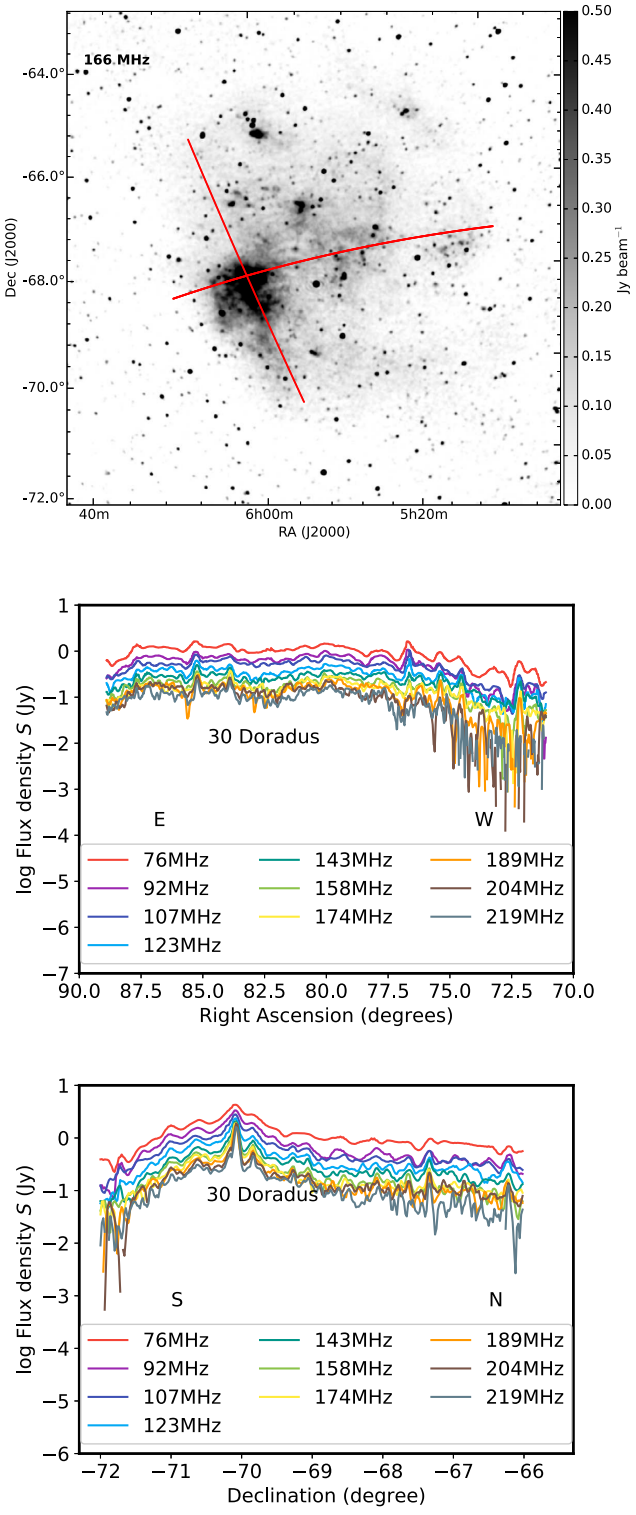

Figure 5. Intensity profiles of the LMC in a logarithmic scale. *Top:* 166 MHz image over $10^\circ \times 10^\circ$. The red lines represent the slice axes in an interval of 0.02° across 30 Doradus for the intensity profiles. The grey scale is in units of Jy beam^{-1}. *Middle:* Intensity profile in east-west direction. *Bottom:* Same as top except for south–north direction.

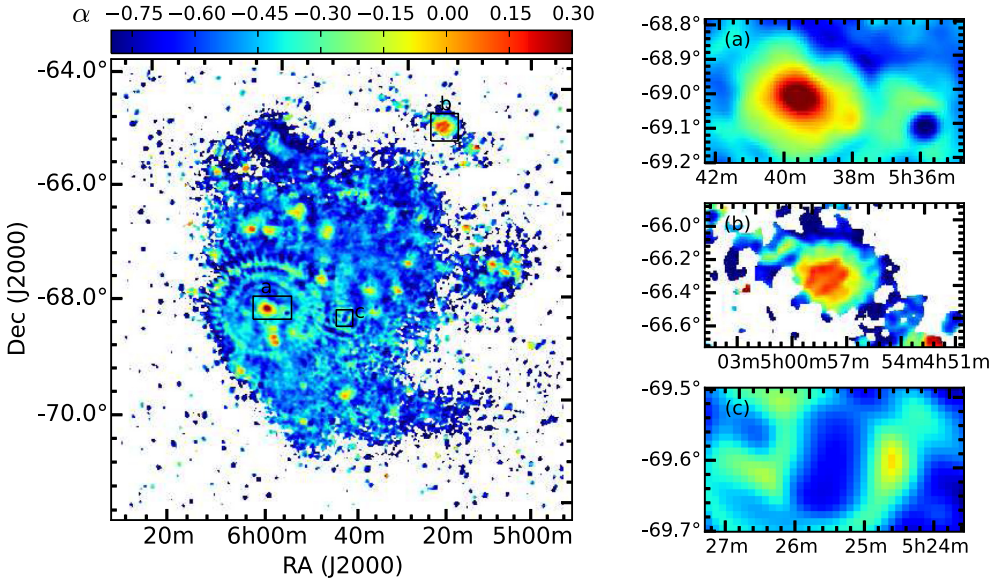

Figure 6. Spectral index map of the LMC calculated from the GLEAM 166 MHz and the 1.4 GHz images. Panels (a) and (b) on the right show HII regions: 30 Doradus and N11. Both have positive α indicating the emission is dominated by thermal emission. At the right corner of panel (a) also shows a prominent source, the supernova remnant 1987A, which has a steep negative α indicating the emission is dominated by non-thermal synchrotron emission. Panel (c) shows supernova remnant N132D. It has a similar α as the supernova remnant 1987A.

The 1.4 GHz images are convolved and regridded to match the resolution and pixel scale of the GLEAM images. Then, the spectral index maps are made measuring

$$\alpha = \log_{10}(S_{\nu_{\rm GLEAM}}/S_{\nu_{1.4\,\rm GHz}})/\log_{10}(\nu_{\rm GLEAM}/1.4\ \rm GHz), \quad (10)$$

for all pixels above 3σ. Fig. 6 shows the variation of spectral indices across the LMC. The H II regions are easily recognized from their radio spectra ($\alpha > -0.1$). We zoom in to show two known HII regions: 30 Doradus and N11, in the right-hand panels (a) and (b). At an angular resolution of ∼3.7 arcmin, both HII regions are not completely resolved at 166 MHz. The supernova remnant N132D as shown in right-hand panel (c) reveals a steep negative spectrum ($\alpha \sim -0.7 \pm 0.02$), which is in good agreement with the derived spectral index ($\alpha = -0.65 \pm 0.04$) from Bozzetto et al. (2017). The steep negative spectrum also indicates the non-thermal synchrotron emission from the shock fronts (Vogt & Dopita 2011). A similar spectrum ($\alpha \sim -0.74 \pm 0.02$) is also derived between 0.072 and 8.64 GHz for SNR 1987A (Callingham et al. 2016).

In the top panels of Fig. 7, we compare the radio spectral index maps with the H_α images (shown in contours) from the Southern H-Alpha Sky Survey Atlas (SHASSA; Gaustad et al. 2001). The H_α images are in units of deciRayleighs (dR), where 1 R = 10^6 photons per 4π steradian = 2.42×10^{-7} ergs cm^{-2} s^{-1} sr^{-1}. They have a resolution of 0.8 arcmin and are convolved and regridded to match the resolution and pixel scale of the radio spectral index maps. Comparison shows a strong correlation between radio spectral index and H_α emission in giant H II regions and star-forming complexes, which potentially also emit non-thermal emission. In Fig. 8, we show a pixel–pixel plot of H_α emission versus spectral index focused on a 6 arcmin × 6 arcmin region around the N66 HII complex in the SMC. The calculated Pearson's correlation coefficient is 0.89. Overlaying the 166 MHz intensity contours on to the H_α images shows the boundary of the diffuse emission at low frequency. There is a lack of diffuse emission in the south-west region of the LMC and the diffuse emission is slightly more extended than the H_α emission (bottom panels of Fig. 7).

5 STAR FORMATION IN THE MAGELLANIC CLOUDS

There are many star formation rate (SFR) indicators, ranging from ultraviolet, optical, infrared to radio wavelength (e.g. Kennicutt 1998; Bell 2003; Wu et al. 2005). Ultraviolet stellar continuum and optical recombination lines (H_α) have been widely used in the past but are both affected by dust attenuation. Efforts to find a better star formation indicator to circumvent the dust attenuation problem have turned to infrared (IR) and radio (e.g. Bell 2003; Calzetti et al. 2007). However, it is cautioned that using IR alone can present issues, such as heating of dust by hot evolved stars, which radiate at IR wavelength (e.g. Kennicutt 1998), and large uncertainties in extrapolation of IR luminosity in intermediate or high-redshift studies (e.g. Chapman et al. 2005). The calibration of SFR using far-IR and radio wavelengths has focused on higher frequency (>1.4 GHz) radio continuum emission. With recent radio continuum studies using low-frequency telescopes, such as LOFAR (Low-Frequency Array; van Haarlem et al. 2013) and MWA, a new spectral window has been opened to investigate SFR using far-IR to radio continuum emission correlation down to 150 MHz (Brown et al. 2017; Calistro Rivera et al. 2017). A comprehensive study to calibrate SFR indicators at different wavelengths on an homogeneous scale has been carried out by Brown et al. (2017), hereafter B17. This study uses the 150 MHz flux densities of sources from the GLEAM catalogue (Hurley-Walker et al. 2017) to calibrate the SFR at low redshift. The LOFAR study provides SFR calibration of 150 MHz in a higher redshift regime (Calistro Rivera et al. 2017).

We employ the 150 MHz–H_α relation in table 4 of B17 to calculate the global SFRs for the LMC and SMC. We find that the resulting SFRs depend on the adopted initial mass function (IMF). Conversions between SFR and the 150 MHz–H_α relation based on the IMF of Salpeter (1955), Kroupa (2001), Chabrier (2003) and Baldry & Glazebrook (2003) are given in B17. For comparison with the literature values, we calculate the global SFRs for the LMC and SMC using above IMFs. This yield 0.106 $M_\odot$ yr^{-1} (LMC) and

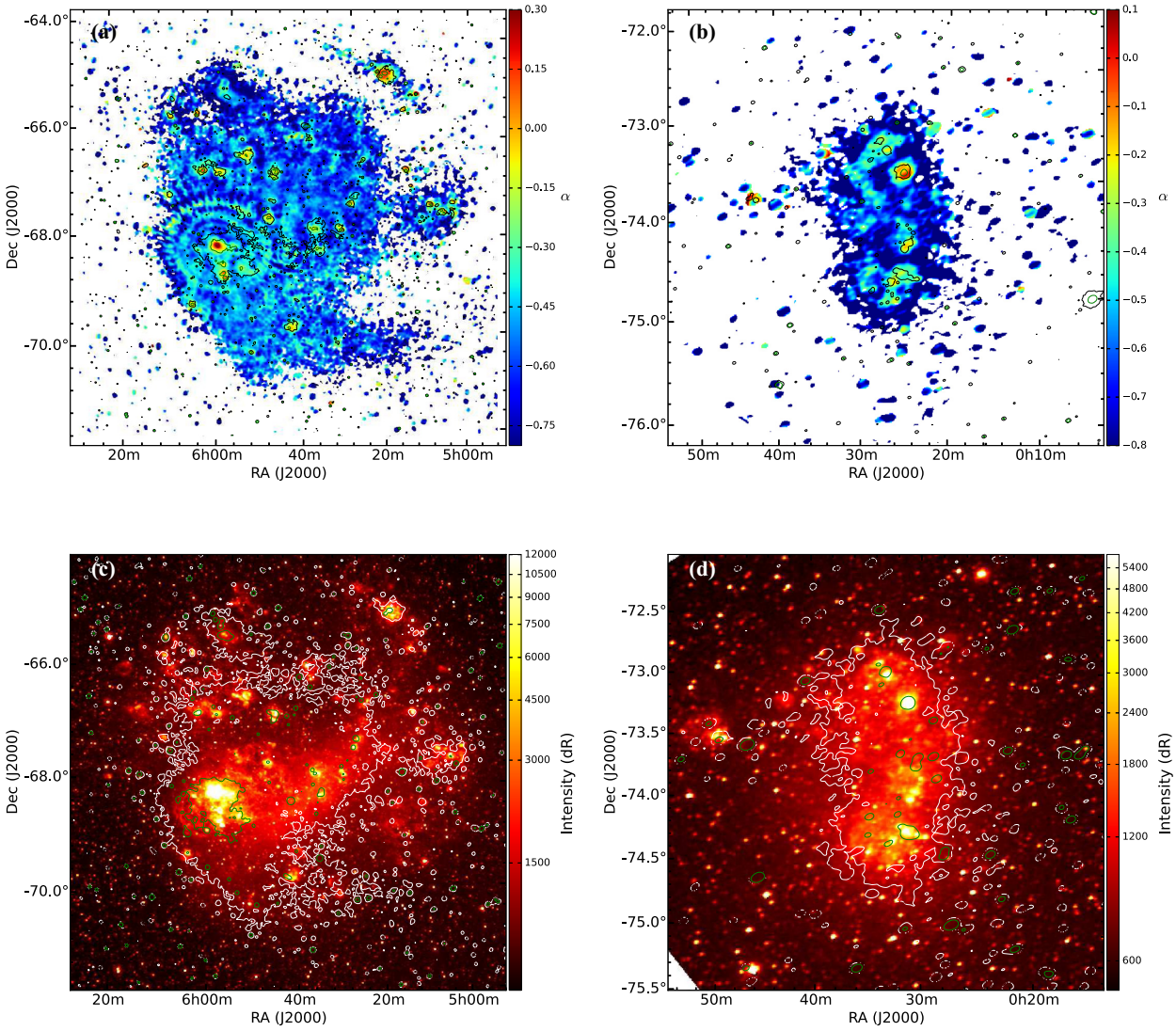

Figure 7. *Top panels*: Contours of H_α at 2500 dR (black) and 10000 dR (green) overlaid on to the spectral index maps. *Bottom panels:* Intensity contours of 166 MHz continuum map at 0.1 Jy beam^{-1} (white) and 0.4 Jy beam^{-1} (green) overlaid on to the SHASSA H_α image.

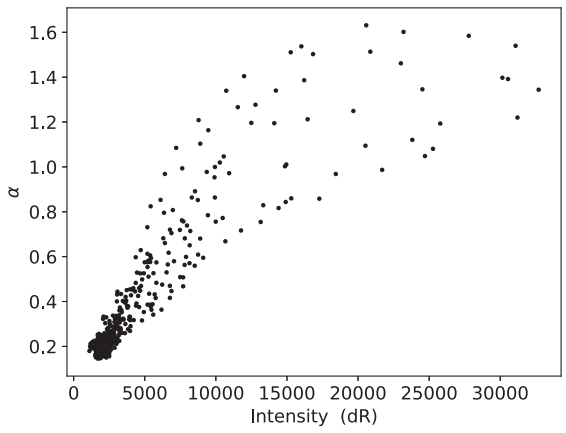

Figure 8. An example of the relationship between H_α emission and spectral index in an H II region (N66) in the SMC.

0.033 $M_\odot$ yr^{-1} (SMC) for the Salpeter IMF, 0.074 $M_\odot$ yr^{-1} (LMC) and 0.022 $M_\odot$ yr^{-1} (SMC) for the Kroupa IMF, 0.161 $M_\odot$ yr^{-1} (LMC) and 0.050 $M_\odot$ yr^{-1} (SMC) for the Chabrier IMF, 0.068 $M_\odot$ yr^{-1} (LMC) and 0.021 $M_\odot$ yr^{-1} (SMC) for the Baldry & Glazebrook IMF. The global SFR for the LMC is about a factor of 2 less than the SFR ($\sim$0.2 $M_\odot$ yr^{-1}) quoted in Hughes et al. (2007), where the Salpeter IMF was used. It is also lower by about a factor of 1.5 as compared to 0.037 $M_\odot$ yr^{-1} in Bolatto et al. (2011), where Kroupa IMF was adopted. The values calculated using Chabrier IMF are more consistent with the literature values that are based on the 1.4 GHz calibration. The SFR is known to be underestimated at low frequencies (see e.g. Calistro Rivera et al. 2017).

6 H II REGIONS

The ionizing Lyman continuum photons from young massive OB stars are the cause of their surrounding HII regions. In these regions, the strong correlation between H_α and radio continuum emission indicates a thermal origin (only $\alpha \sim -0.1$). Pellegrini et al. (2012)

Table 5. Lower limit of Lyman continuum photon production rates of selected H II regions in the LMC with $\alpha > 0$ (see section 6.1).

Source	MCELS ID	R.A. (J2000) (h:m:s)	Decl. (J2000) (° arcmin arcsec)	N_{UV} (s^{-1})	α
H II 1	L102	05:05:06.7	−70:06:24.1	7.70×10^{50}	–
H II 2	L106	05:06:05.0	−65:41:28.7	1.46×10^{51}	–
H II 3	L119	05:09:34.3	−68:53:44.9	1.40×10^{51}	0.05 ± 0.03
H II 4	L134	05:12:28.4	−70:24:52.2	2.51×10^{51}	–
H II 5	L201	05:22:06.9	−67:56:46.0	3.74×10^{51}	0.04 ± 0.03
H II 6	L258	05:26:42.5	−68:49:34.0	2.52×10^{51}	0.12 ± 0.04
H II 7	L260	05:27:17.6	−70:34:46.2	8.74×10^{50}	–
H II 8	L307	05:35:15.6	−67:34:04.1	1.88×10^{51}	0.09 ± 0.03
H II 9	L328	05:38:36.0	−69:05:10.7	1.06×10^{52}	–
H II 10	L343	05:40:06.8	−69:45:28.4	2.64×10^{51}	0.09 ± 0.03

carried out a study of the optical depth H II regions in the MCs using the images from the Magellanic Clouds Emission Line Survey (MCELS; Smith & MCELS Team 1998). The study categorized the HII regions into several groups, including optically thin and thick. Using the catalogue of Pellegrini et al. (2012), we first examined H II regions that are classified as optically thin. If they appear to be point sources or not complex at 150 MHz, we extract them as cutout images. This results in 46 H II regions for the LMC and 2 H II regions for the SMC. Subsequently, we obtain their integrated flux densities by fitting a two-dimensional Gaussian to these cutout images. Only 10 out of the 46 H II regions in the LMC have converged Gaussian fits, and none for the SMC. The fitting fails to converge if the sources appear to have multiple components. The derived S_ν are used to calculate the production rate of Lyman continuum photons (N_{UV}) in the optically thin regime. In this regime, the thermal spectral luminosity (L_T) of an H II region is proportional to the production rate of Lyman continuum photons and varies weakly with electron temperature (T_e) (Rubin 1968). According to Condon (1992), the value of N_{UV} (s^{-1}) can be estimated from

$$\frac{N_{UV}}{s} \gtrsim 6.3 \times 10^{52} \left(\frac{T_e}{10^4 \mathrm{K}}\right)^{-0.45} \left(\frac{\nu}{\mathrm{GHz}}\right)^{0.1} \left(\frac{L_T}{10^{20}\ \mathrm{W\ Hz^{-1}}}\right). \quad (11)$$

We assume T_e to be 10^4 K and note that equation (4) is only applicable to H II regions that are solely thermal. This equation also yields a lower limit of N_{UV} due to some Lyman continuum photons being absorbed by dust within the H II regions. The result is shown in Table 5. Among these H II regions, the largest star-forming region in the LMC, 30 Doradus (source HII 9), has the highest N_{UV}. The N_{UV} values for the rest of them are of the order of $\sim 10^{51}$ s^{-1}, which is about 10 times higher than the N_{UV} of H II regions in the irregular dwarf galaxy IC 10 (Westcott et al. 2017). A correlation between ionizing UV flux and radio flux densities for the LMC HII regions has also been found (see Filipovic, Jones & White 2003).

Studying γ-ray emission in the MCs allows us to probe the physical processes of cosmic rays (CRs) interaction with the interstellar medium (Ackermann et al. 2016). Discrete sources, in particularly the star-forming regions, are claimed to be possible sites for producing large amount of CR-induced γ-ray emission. While we are not focusing on this topic in this paper, we can estimate the CR confinement within the LMC and SMC by comparing the contribution from discrete sources to the total S_ν. The total integrated flux density of 10 H II regions listed above is ∼138 Jy at 150 MHz, which includes the largest H II region (30 Doradus). Based on the LMC discrete sources listed in Filipovic et al. (2003), we measure their S_ν and yields a total S_ν of ∼163 Jy. As for the SMC, we focus on the H II regions in Pellegrini et al. (2012) and SNRs in Bozzetto et al. (2017). The total S_ν from the SMC discrete sources is ∼59 Jy. These yield ∼21 per cent and ∼23 per cent of the emission attributed to individual sources at 150 MHz for the LMC and SMC, respectively.

6.1 T–T plot

To investigate a possible spatial variation of the spectral index across the resolved H II regions in both 227 MHz and 1.4 GHz images, we use the T–T method (Turtle et al. 1962). This method compares flux density (or brightness temperature) at two frequencies from different instruments and allows for possible foreground contamination as well as variations due to short spacings. If there is any difference in short spacings or contamination from foreground emission, it will result in a non-zero intercept in the T–T plot. We generate the T–T plot by convolving and regridding the LMC 1.4 GHz image to match the angular resolution and pixel scale of the 227 MHz GLEAM image. The 227 MHz GLEAM image is chosen because it has the highest angular resolution. Subsequently, we subsample the data points per 5 pixel (∼1.3 beam separation) in the image plane to remove pixel-to-pixel correlations. Then, we fit the subsampled data using linear least squares regression. The spectral index is then determined by $\alpha = \log(\text{slope})/c$, where c is log (227 MHz/1400 MHz). We present the T–T plots in Fig. 9 and summarize the derived spectral indices in Table 5. All fits yield an overall $R^2 = 0.93$, which suggests no spatial variation of the spectral index across these H II regions. We cannot derive spectral indices for five of the H II regions using the T–T method because the sources are resolved at 1.4 GHz (multiple components) but not resolved in 227 MHz or affected by artefacts at 1.4 GHz (near the 30 Doradus region). The derived spectral indices of these HII regions ranges from ∼0.0 to ∼0.1, which suggests a "flat" spectrum dominated by thermal emission. These H II regions are in the optically thin regime in the MWA frequency range. We also attempted to derive the spectral index and to identify the turn-over frequency using the optically thick H II regions defined in the catalogue of Pellegrini et al. (2012). However, we do not see any convincing evidence of a turn over frequency due to difficulty in measuring accurate flux densities in the lower MWA frequency bands as a result of poor resolution.

7 CONCLUSIONS

We present a low-frequency radio continuum study of the Magellanic Clouds as part of the GLEAM survey. The intensity of the radio continuum emission is correlated with H I column density. Star-forming regions are the main contributors to the

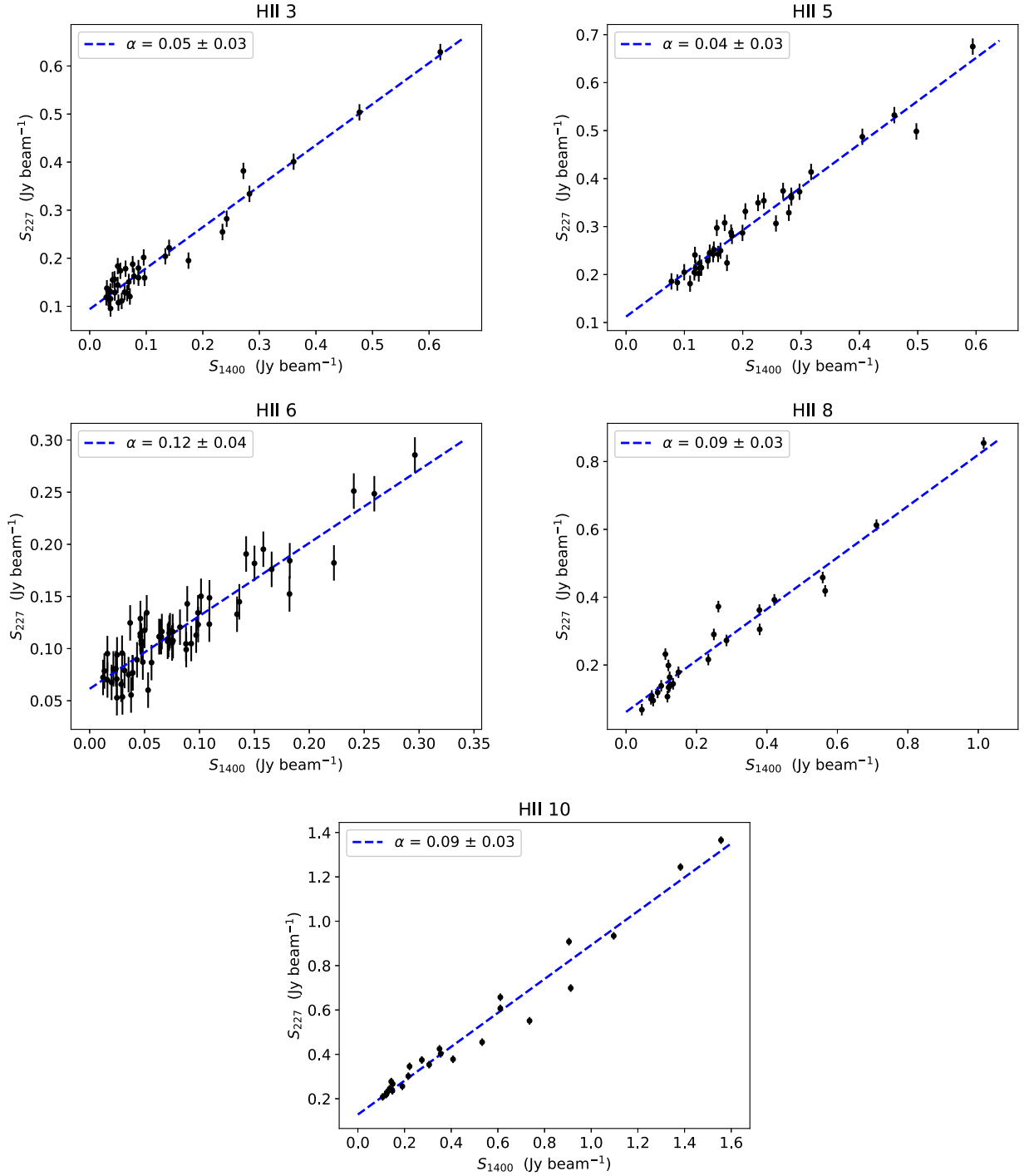

Figure 9. T–T plots for the five optically thin HII regions in the LMC using 1.4 GHz and 227 MHz images. The 1.4 GHz cutout images have been convolved and regridded to match the resolution and pixel scale of the 227 MHz images. The data points have been subsampled every 5 pixel in the image plane. The fitted lines are the spectral indices of these regions. Error of S_{1400} is ∼0.3 mJy beam^{-1}, which makes the error bars too small to be visible in these plots.

emission. Intensity variation is noticeable in the LMC but flat across the bar of the SMC. We derive spectral indices of the MCs using 200 MHz as a reference frequency. A double power-law model is required to fit the SED of the LMC. The fitted model yields $\alpha_0 = -0.66 \pm 0.08$ (non-thermal) when α_1 (thermal) is fixed at -0.1. A power-law model is preferred for the SMC, which yields $\alpha_{8.55\mathrm{GHz}}^{85.5\mathrm{MHz}}$ (SMC) $= -0.82 \pm 0.03$. Spectral index maps show a variation of α across the Magellanic Clouds, which reflects the presence of thermal and non-thermal components. H II regions have a distinctive flat spectral index and strongly correlate with H_α, indicating mainly thermal emission. We also calculate the lower limit production rate of Lyman continuum photons of ten HII regions in the LMC using their integrated flux density at 150 MHz. An investigation of spectral index variation among the H II regions is carried out using the T–T method. The derived spectral indices for these HII regions are between about 0 and 0.1. The new H_α–150 MHz SFR calibrations

(Brown et al. 2017) allow us to determine the global SFRs of the MCs. Using their calibrations based on Salpeter, Kroupa, Chabrier and Baldry & Glazebrook's IMFs, we obtain the global SFRs of 0.068–0.161 $M_\odot$ yr^{-1} and 0.021–0.050 $M_\odot$ yr^{-1} for the LMC and SMC, respectively. We find that the global SFRs are consistent with the 1.4 GHz SFR calibration if Charbrier's IMF is adopted. Robust -1 images in 20 frequency bands and wideband averages are made available at the GLEAM Virtual Observatory (VO) server.[2]

8 FUTURE WORK

A detailed study of discrete sources such as H II regions, supernova remnants, and background sources in the GLEAM images will be presented in a subsequent paper. An analysis of the radio-FIR correlation has been performed in the past for the MCs (Hughes et al. 2006; Leverenz & Filipović 2013). These studies focused on 1.4 GHz and Infrared Astronomical Satellite (IRAS) images. Future work includes an investigation of the radio-FIR correlation on different spatial scales using MWA and Herschel images (as part of the HERschel Inventory of The Agents of Galaxy Evolution survey; HERITAGE; Meixner et al. 2013). A deep survey of the Magellanic System (MAGE-X; led by L. Staveley-Smith) using the MWA phase II system has been commenced. The survey will focus on quantifying the energy spectrum of cosmic ray electrons at higher angular resolution.

ACKNOWLEDGEMENTS

This scientific work makes use of the Murchison Radio-astronomy Observatory, operated by CSIRO. We acknowledge the Wajarri Yamatji people as the traditional owners of the Observatory site. Support for the operation of the Murchison Widefield Array is provided by the Australian Government (NCRIS), under a contract to Curtin University administered by Astronomy Australia Limited. We acknowledge the Pawsey Supercomputing Centre which is supported by the Western Australian and Australian Governments and the Centre of Excellence for All-sky Astrophysics (CAASTRO), which is an Australian Research Council Centre of Excellence, funded by grant CE110001020. Parts of this research were conducted with the support of Australian Research Council Centre of Excellence for All Sky Astrophysics in 3 Dimensions (ASTRO 3D), through project number CE170100013. This research also made use of Montage. Montage is funded by the National Science Foundation under Grant Number ACI-1440620, and was previously funded by the National Aeronautics and Space Administration's Earth Science Technology Office, Computation Technologies Project, under Cooperative Agreement Number NCC5-626 between NASA and the California Institute of Technology.

REFERENCES

Ackermann M. et al., 2016, A&A, 586, A71
Alvarez H., Aparici J., May J., 1987, A&A, 176, 25
Baars J. W. M., Genzel R., Pauliny-Toth I. I. K., Witzel A., 1977, A&A, 61, 99
Baldry I. K., Glazebrook K., 2003, ApJ, 593, 258
Bell E. F., 2003, ApJ, 586, 794
Besla G., Martínez-Delgado D., van der Marel R. P., Beletsky Y., Seibert M., Schlafly E. F., Grebel E. K., Neyer F., 2016, ApJ, 825, 20
Blackburn J. K., 1995, in Shaw R. A., Payne H. E., Hayes J. J. E., eds, ASP Conf. Ser. Vol. 77, Astronomical Data Analysis Software and Systems IV. Astron. Soc. Pac., San Francisco, p. 367
Bolatto A. D., Leroy A., Israel F. P., Jackson J. M., 2003, ApJ, 595, 167
Bolatto A. D. et al., 2011, ApJ, 741, 12
Bowman J. D. et al., 2013, PASA, 30, e031
Bozzetto L. M. et al., 2017, ApJS, 230, 2
Briggs D. S., 1995, Bull. Am. Astron. Soc., 27, 1444
Brown M. J. I. et al., 2017, *ApJ*, 847, 136 (B17)
Brüns C. et al., 2005, A&A, 432, 45
Calistro Rivera G. et al., 2017, MNRAS, 469, 3468
Callingham J. R. et al., 2016, MNRAS, 462, 290
Calzetti D. et al., 2007, ApJ, 666, 870
Chabrier G., 2003, PASP, 115, 763
Chapman S. C., Blain A. W., Smail I., Ivison R. J., 2005, ApJ, 622, 772
Chen C.-H. R. et al., 2014, ApJ, 785, 162
Condon J. J., 1992, ARA&A, 30, 575
Diaz J., Bekki K., 2011, PASA, 28, 117
Feitzinger J. V., Perschke M., Haynes R. F., Klein U., Wielebinski R., 1987, Vistas in Astron., 30, 243
Filipovic M. D., Haynes R. F., White G. L., Jones P. A., 1998, A&AS, 130, 421
Filipović M. D., Bohlsen T., Reid W., Staveley-Smith L., Jones P. A., Nohejl K., Goldstein G., 2002, MNRAS, 335, 1085
Filipovic M. D., Jones P. A., White G. L., 2003, Serb. Astron. J., 166
Gaustad J. E., McCullough P. R., Rosing W., Van Buren D., 2001, PASP, 113, 1326
Harris J., 2007, ApJ, 658, 345
Harvey V. M., Franzen T., Morgan J., Seymour N., 2018, MNRAS, 476, 2717
Haslam C. G. T., Klein U., Salter C. J., Stoffel H., Wilson W. E., Cleary M. N., Cooke D. J., Thomasson P., 1981, A&A, 100, 209
Haynes R. F. et al., 1991, A&A, 252, 475
Helou G., Bicay M. D., 1993, ApJ, 415, 93
Hilditch R. W., Howarth I. D., Harries T. J., 2005, MNRAS, 357, 304
Hughes A., Wong T., Ekers R., Staveley-Smith L., Filipovic M., Maddison S., Fukui Y., Mizuno N., 2006, MNRAS, 370, 363
Hughes A., Staveley-Smith L., Kim S., Wolleben M., Filipović M., 2007, MNRAS, 382, 543
Hurley-Walker N. et al., 2017, MNRAS, 464, 1146
Jameson K. E. et al., 2016, ApJ, 825, 12
Kallivayalil N., van der Marel R. P., Besla G., Anderson J., Alcock C., 2013, ApJ, 764, 161
Kass R. E., Raftery A. E., 1995, J. Am. Stat. Assoc., 90, 773
Kennicutt R. C., Jr, 1998, ARA&A, 36, 189
Kim S., Staveley-Smith L., Dopita M. A., Sault R. J., Freeman K. C., Lee Y., Chu Y.-H., 2003, ApJS, 148, 473
Klein U., Wielebinski R., Haynes R. F., Malin D. F., 1989, A&A, 211, 280
Kroupa P., 2001, MNRAS, 322, 231
Leverenz H., Filipović M. D., 2013, Ap&SS, 343, 301
Lisenfeld U., Völk H. J., 2000, A&A, 354, 423
Loiseau N., Klein U., Greybe A., Wielebinski R., Haynes R. F., 1987, A&A, 178, 62
Lonsdale C. J. et al., 2009, IEEE Proceedings, 97, 1497
Mackey A. D., Koposov S. E., Erkal D., Belokurov V., Da Costa G. S., Gómez F. A., 2016, MNRAS, 459, 239
Marvil J., Owen F., Eilek J., 2015, AJ, 149, 32
Meixner M. et al., 2013, AJ, 146, 62
Mills B. Y., 1955, Aust. J. Phys., 8, 368
Mills B. Y., 1959, Handbuch der Physik, 53, 239
Mountfort P. I., Jonas J. L., de Jager G., Baart E. E., 1987, MNRAS, 226, 917
Ochsendorf B. B., Zinnecker H., Nayak O., Bally J., Meixner M., Jones O. C., Indebetouw R., Rahman M., 2017, Nature Astron., 1, 268
Offringa A. R. et al., 2015, PASA, 32, e008
Pellegrini E. W., Oey M. S., Winkler P. F., Points S. D., Smith R. C., Jaskot A. E., Zastrow J., 2012, ApJ, 755, 40
Pietrzyński G. et al., 2013, Nature, 495, 76

[2] http://gleam-vo.icrar.org/gleam_postage/q/form

Rubin R. H., 1968, ApJ, 154, 391
Salpeter E. E., 1955, ApJ, 121, 161
Schwarz G., 1978, Ann. Statist., 5, 461
Shain C. A., 1959, in Bracewell R. N., ed., IAU Symp. 9, Observations of Extragalactic Radio Emission. Stanford Univ. Press, Stanford, CA, p. 328
Smith R. C., MCELS Team, 1998, PASA, 15, 163
Stanimirovic S., Staveley-Smith L., Dickey J. M., Sault R. J., Snowden S. L., 1999, MNRAS, 302, 417
Staveley-Smith L., Sault R. J., Hatzidimitriou D., Kesteven M. J., McConnell D., 1997, MNRAS, 289, 225
Staveley-Smith L., Kim S., Calabretta M. R., Haynes R. F., Kesteven M. J., 2003, MNRAS, 339, 87
Tingay S. J. et al., 2013, PASA, 30, e007
Turtle A. J., Pugh J. F., Kenderdine S., Pauliny-Toth I. I. K., 1962, MNRAS, 124, 297
van der Marel R. P., Kallivayalil N., 2014, ApJ, 781, 121
van Haarlem M. P. et al., 2013, A&A, 556, A2
Vogt F., Dopita M. A., 2011, Ap&SS, 331, 521
Wayth R. B. et al., 2015, PASA, 32, e025
Westcott J. et al., 2017, MNRAS, 467, 2113
Wu H., Cao C., Hao C.-N., Liu F.-S., Wang J.-L., Xia X.-Y., Deng Z.-G., Young C. K.-S., 2005, ApJ, 632, L79
Zanardo G. et al., 2010, ApJ, 710, 1515

[1]*International Centre for Radio Astronomy Research, University of Western Australia, 35 Stirling Hwy, Crawley, WA 6009, Australia*
[2]*ARC Centre of Excellence for All Sky Astrophysics in 3 Dimensions (ASTRO 3D)*
[3]*ARC Centre of Excellence for All-sky Astrophysics (CAASTRO)*
[4]*International Centre for Radio Astronomy Research, Curtin University, Bentley, WA 6102, Australia*
[5]*National Radio Astronomy Observatory (NRAO), Socorro, NM 87801, USA*
[6]*School of Computing Engineering and Mathematics, Western Sydney University, Locked Bag 1797, Penrith, NSW 2751, Australia*
[7]*CSIRO Astronomy and Space Science (CASS), PO Box 76, Epping, NSW 1710, Australia*
[8]*The Inter-University Institute for Data Intensive Astronomy (IDIA), Department of Astronomy, University of Cape Town, Rondebosch, 7701, South Africa*
[9]*Netherlands Institute for Radio Astronomy (ASTRON), Dwingeloo, the Netherlands*
[10]*University of Technology Sydney, 15 Broadway, Ultimo NSW 2007, Australia*
[11]*Department of Physics and Electronics, Rhodes University, PO Box 94, Grahamstown 6140, South Africa*
[12]*School of Earth and Space Exploration, Arizona State University, Tempe, AZ 85287, USA*
[13]*Research School of Astronomy and Astrophysics, Australian National University, Canberra, ACT 2611, Australia*
[14]*MIT Haystack Observatory, Westford, MA 01886, USA*
[15]*Raman Research Institute, Bangalore 560080, India*
[16]*Dunlap Institute for Astronomy and Astrophysics, University of Toronto, ON, M5S 3H4, Canada*
[17]*Sydney Institute for Astronomy, School of Physics, The University of Sydney, NSW 2006, Australia*
[18]*Harvard-Smithsonian Center for Astrophysics, Cambridge, MA 02138, USA*
[19]*Department of Physics, University of Washington, Seattle, WA 98195, USA*
[20]*Centre for Astrophysics Research, School of Physics, Astronomy and Mathematics, University of Hertfordshire, College Lane, Hatfield AL10 9AB, UK*
[21]*Peripety Scientific Ltd., PO Box 11355 Manners Street, Wellington 6142, New Zealand*
[22]*Department of Physics, University of Wisconsin–Milwaukee, Milwaukee, WI 53201, USA*
[23]*School of Physics, The University of Melbourne, Parkville, VIC 3010, Australia*
[24]*Kavli Institute for Astrophysics and Space Research, Massachusetts Institute of Technology, Cambridge, MA 02139, USA*
[25]*National Centre for Radio Astrophysics, Tata Institute for Fundamental Research, Pune 411007, India*
[26]*School of Engineering & Computer Science, Victoria University of Wellington, PO Box 600, Wellington 6141, New Zealand*

This paper has been typeset from a TEX/LATEX file prepared by the author.